

New Binary Black Hole Mergers in the Second Observing Run of Advanced LIGO and Advanced Virgo

Tejaswi Venumadhav,^{1,*} Barak Zackay,¹ Javier Roulet,² Liang Dai,¹ and Matias Zaldarriaga¹

¹*School of Natural Sciences, Institute for Advanced Study, 1 Einstein Drive, Princeton, NJ 08540, USA*

²*Department of Physics, Princeton University, Princeton, NJ, 08540, USA*

(Dated: April 16, 2019)

We report the detection of new binary black hole merger events in the publicly available data from the second observing run of advanced LIGO and advanced Virgo (O2). The mergers were discovered using the new search pipeline described in Venumadhav *et al.* [1], and are above the detection thresholds as defined in Abbott *et al.* [2]. Three of the mergers (GW170121, GW170304, GW170727) have inferred probabilities of being of astrophysical origin $p_{\text{astro}} > 0.98$. The remaining three (GW170425, GW170202, GW170403) are less certain, with p_{astro} ranging from 0.5 to 0.8. The newly found mergers largely share the statistical properties of previously reported events, with the exception of GW170403, the least secure event, which has a highly negative effective spin parameter χ_{eff} . The most secure new event, GW170121 ($p_{\text{astro}} > 0.99$), is also notable due to its inferred negative value of χ_{eff} , which is inconsistent with being positive at the $\approx 95.8\%$ confidence level. The new mergers nearly double the sample of gravitational wave events reported from O2, and present a substantial opportunity to explore the statistics of the binary black hole population in the Universe. The number of detected events is not surprising since we estimate that the detection volume of our pipeline is nearly twice that of other pipelines. The increase in volume is larger when the constituent detectors of the network have very different sensitivities, as is likely to be the case in current and future runs.

I. INTRODUCTION

The LIGO–Virgo Collaboration (LVC) reported the detection of gravitational waves from ten binary black hole (BBH) and one binary neutron star mergers in their two latest observing runs, O1 and O2 [2–9]. The intrinsic properties of the mergers, namely the masses, the mass ratio and the spins of the black holes, are important observables that can inform us about how and where the binaries were assembled. All the BBH events are consistent with mergers of black holes with comparable masses (notably, GW170729 is mildly inconsistent with equal component masses [10]); in two of the events, at least one of the components had a nonzero spin.

Currently, inference about the origin of the BBHs is limited by the small number of detected events. Future observations with improved sensitivity will enlarge the sample and map out the parameter space of the BBH population; meanwhile, it is important to adopt analysis techniques that maximize the yield of existing data.

A number of data analysis pipelines have been developed to search for transient events in LIGO–Virgo data. The two standard modeled searches used by the LVC are PyCBC [11] and GstLAL [12]; these pipelines use matched filtering with a template bank of target compact binary coalescence signals. In addition, the LVC runs an unmodeled transient search with the coherent Wave Burst pipeline [13]. There are also groups external to the LVC running independent pipelines [1, 14] on the public data released by the LVC, which now includes the O1 and O2

observing runs [15, 16]. In Ref. [1] we presented a new and independent pipeline to analyze public LIGO data, which we applied to the public data from the O1 observing run. The cumulative improvements significantly increased the sensitive volume (at the same detection thresholds as those of Ref. [2]), and led to the detection of a new event, which is consistent with the merger of rapidly spinning and heavy black holes [17]. In this paper, we present results from our search of coincident triggers in the Hanford (H1) and Livingston (L1) public data from the second observing run of advanced LIGO (O2) [15, 16].

The paper is organized as follows: in Section II we describe the changes in the pipeline used in this paper compared the one used to analyze the O1 data. Section III summarizes the results of our analysis on the events that were previously detected by the LVC analysis pipelines in Ref. [2]. We describe the new events we found in Section IV, estimate our improvement in sensitivity in Section V, and conclude with some remarks in Section VI. In Appendices A–C, we present the posterior distributions for the parameters of the new events, as well as some technical details.

II. CHANGES TO THE O1 ANALYSIS PIPELINE

Our analysis pipeline is similar in overall structure to the one we used in the O1 analysis [1]. In detail, the pipeline for the O2 analysis differs in the following aspects:

1. *Construction of the template bank:* We use the template bank described in [18]. As in the O1 analysis,

* tejaswi@ias.edu

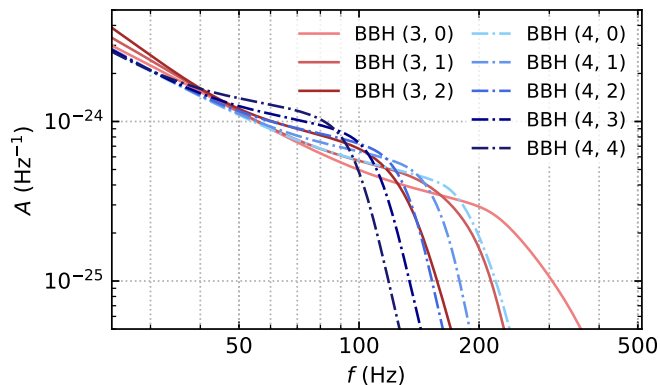


FIG. 1: Sub-bank amplitude profiles as a function of frequency f for banks BBH 3 and BBH 4.

we divide our BBH search into five banks (BBH 0–4) based on the chirp masses of the templates, and divide each bank into sub-banks based on the shape of the frequency-domain amplitude profile. We now use the k -means algorithm to automatically divide each bank into sub-banks, each of which has a frequency-domain amplitude, $\bar{A}(f)$, that is the root-mean-square average of the amplitudes of the constituent astrophysical waveforms. In Fig. 1 we show $\bar{A}(f)$ for all the sub-banks in our banks covering detector chirp masses 20–40 M_{\odot} (bank BBH 3) and above 40 M_{\odot} (BBH 4). All the events we report in this paper fall in these banks.

The phases of the templates are linear combinations of basis functions, $\psi_{\alpha}(f)$, whose form depends on the noise power spectral density (PSD); we use the PSD estimated from a representative set of files from the run (instead of a model PSD as was done in the O1 analysis). We also restrict the templates to frequencies between 24 and 512 Hz. Cumulatively, these changes enable us to cover the same astrophysical parameter space using $\sim 30\%$ fewer templates, and achieve slightly better effectiveness [18].

2. *Preprocessing and flagging the data:* Our analysis pipeline produces a stream of whitened data per 4096 s file. We perform several tests on the data to identify prolonged or transient disturbances in the detector that appear as segments with excess power, and discard these segments to avoid polluting our search. We would like these tests not to trigger on astrophysical signals of interest. Towards this end, in our previous analysis we set the threshold for each test to the power achieved in the absence of noise by signals with a fiducial signal-to-noise ratio $(\text{SNR})_{\text{max}}$. In the presence of noise, real signals with $\text{SNR} < (\text{SNR})_{\text{max}}$ can have excess power above these thresholds due to upward fluctuations. Hence, in our O1 analysis we used a relatively high value of $(\text{SNR})_{\text{max}} = 30$ to ensure

completeness at lower values [1].

A better design for tests would be to ensure a given false-positive probability for signals with a desired signal-to-noise ratio. For whitened data, power in a given band, and on a given timescale, is distributed according to a non-central chi-squared distribution in the presence of a signal; hence, we can set thresholds such that signals with a given value of $(\text{SNR})_{\text{max}}$ are flagged with a probability $< 10^{-4}$. Given this promise, we lower the target value to $(\text{SNR})_{\text{max}} = 20$.

3. *Refining coincident triggers:* The phases of our templates belong to a vector space, \mathcal{V} , spanned by the basis functions $\{\psi_{\alpha}(f) : \alpha = 1, 2 \dots n\}$; the template bank is a discrete subset of this space with basis coefficients that live on an n -dimensional grid. We determine the extent of the grid in all dimensions by projecting a large random sample of astrophysical waveforms into \mathcal{V} and ensuring that every waveform has a nearby grid point. We allow comparatively large mismatches ($\lesssim 10\%$) between astrophysical waveforms and the best template in the bank, which enables us to work with coarser grids on \mathcal{V} when generating triggers. We then reduce the mismatch for significant triggers by refining their coefficients on a finer local grid. In the O1 analysis, we chose this grid to be a uniform regular grid centered on a trigger of interest [1].

For heavy BBH waveforms, the set \mathcal{S} of projected astrophysical waveforms is typically thin and mildly curved in higher dimensions ($\alpha \gtrsim 2$) [18]. The strategy used in the O1 analysis can cause us to step outside \mathcal{S} in these dimensions, and introduce unphysical degrees of freedom that pick up noise but no signal. In this analysis, we change the spacing of the finer grid and excise unnecessary elements to ensure that we enumerate over templates within \mathcal{S} . Note that different choices of how this refinement is done can lead to different quoted SNRs for the same astrophysical signal depending on how closely the finer grid approaches it. Hence, we apply the same strategy to the background triggers (found via time slides) to avoid biasing the calculation of false-alarm rates (FARs).

4. *Reducing cross-contamination between banks:* High SNR triggers tend to appear in several of our chirp-mass banks, both in the time slides used to estimate our background, as well as in the set of coincident triggers. In the O1 analysis, we assigned triggers to the best sub-bank in a given chirp-mass bank (as determined by the incoherent network $\text{SNR}^2 = \rho_{\text{H}}^2 + \rho_{\text{L}}^2$, where ρ_{H}^2 and ρ_{L}^2 are the incoherent squared SNRs in Hanford and Livingston, respectively), but allowed them to appear in multiple banks [1]. This choice was conservative, in that it caused us to overestimate the FAR for real events.

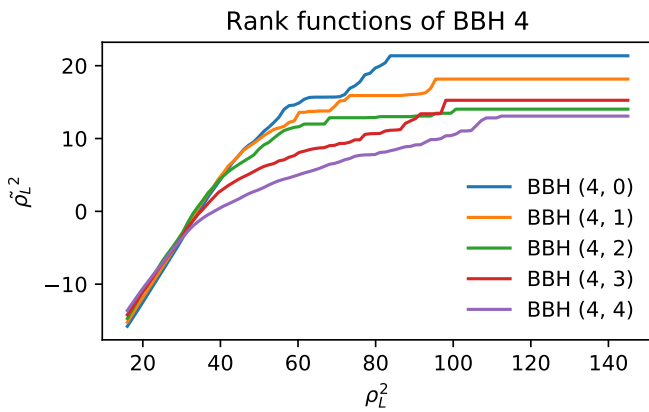


FIG. 2: Rank functions for all sub-banks in bank BBH 4. The different sub-banks have substantially different background rates: glitches prefer the higher-mass sub-banks and, even in the Gaussian part, the slopes may differ due to the different number of degrees of freedom.

In this analysis, we improve upon this in two ways: we assign both background and coincident triggers to a unique bank (and sub-bank within), and instead of the incoherent network SNR², we use a discriminator that better accounts for the different structures of the sub-banks. Appendix B contains the expression (see Eq. (B7)), and outlines a derivation.

5. *Computing the false-alarm rate:* After collecting triggers and assigning them to banks, we estimate the FAR for a given coincident trigger by comparing it to the background triggers (collected using time slides) within the same chirp-mass bank. Our statistic for comparing triggers is the coherent score [19], which for a given trigger t is an approximation of the likelihood ratio under the signal ($\mathcal{L}(t | \mathcal{S})$) and noise ($\mathcal{L}(t | \mathcal{N})$) hypotheses. In the O1 analysis, when estimating $\mathcal{L}(t | \mathcal{N})$, we assumed that the background rate per template is flat over all sub-banks in a given bank [1]. However, we empirically see that the various sub-banks have substantially different background-rates per template. If we do not account for this, a sub-bank with more glitches can disproportionately influence the background in the search.

In order to estimate $\mathcal{L}(t | \mathcal{N})$, we approximated the distribution of background triggers in each detector (as a function of SNR²) by its survival function, or complementary cumulative distribution function, which in turn we obtained empirically by ranking triggers as a function of SNR² in that detector. In this analysis, we separately rank triggers in each sub-bank. Figure 2 shows the rank functions for the five sub-banks of the bank BBH 4 as a function of the SNR² in L1, ρ_L^2 . The distributions of ρ_L^2 transition from exponential (chi-squared-like) to power-

laws when glitches become important, and hence the rank functions flatten: this happens at progressively lower values of ρ_L^2 for higher-mass sub-banks. Moreover, even at low values of ρ_L^2 (in the Gaussian-noise-dominated regime), the rank functions have different slopes in different sub-banks; this is due to the maximization over templates when we collect triggers (see Appendix B for a derivation in a different context).

We compute FARs over all templates in a chirp-mass bank (which is the union of several sub-banks), and hence we need to fix the normalization of the rank functions when comparing triggers from different sub-banks. Appendix C describes the procedure; the rank functions shown in Fig. 2 were normalized in this way.

6. *Computing p_{astro} :* We define $\mathcal{R}(\text{event} | \mathcal{N})$ and $\mathcal{R}(\text{event} | \mathcal{S})$ to be the rates of a given event under the noise (\mathcal{N}) and signal (\mathcal{S}) hypotheses. The probability that an event is astrophysical is

$$p_{\text{astro}}(\text{event}) = \frac{\mathcal{R}(\text{event} | \mathcal{S})}{\mathcal{R}(\text{event} | \mathcal{N}) + \mathcal{R}(\text{event} | \mathcal{S})}. \quad (1)$$

We define a rate \mathcal{R} for each bank to be the overall number of astrophysical events satisfying $\rho_H^2, \rho_L^2 > 16$ and $\rho_H^2 + \rho_L^2 > \rho_{\text{th}}^2$, where $\rho_{\text{th}}^2 = 60$ (58) is the threshold at which we collect coincident triggers in the BBH 3 (BBH 4) bank. The rate \mathcal{R} is for a hypothetical network consisting of two identical detectors, each having a sensitivity equal to the median Hanford sensitivity in the O2 run, which observe in coincidence for 118 days. The assumed rate is assumed to be uniform across templates within the bank, regardless of which sub-bank they might fall in. For a given event, we have

$$\mathcal{R}(\text{event} | \mathcal{S}) = W(\text{event})\mathcal{R}, \quad (2)$$

where the factor W depends on the instantaneous sensitivities of the detectors, as well as the extrinsic parameters of the event. Note that W does not depend on the (unknown) astrophysical rate. We determine the terms in Eqs. (1) and (2) in a similar manner to that of our O1 analysis [1], but with two changes. Firstly, we estimate the rate of producing triggers under the noise hypothesis, $\mathcal{R}(\text{event} | \mathcal{N})$, using only the background triggers in the respective sub-banks that the candidates belong to. Secondly, we determine the rate of astrophysical events, \mathcal{R} , from the data itself rather than assuming it.

Given a particular value of the rate \mathcal{R} , the likelihood of the data is

$$\mathcal{L}(\text{data} | \mathcal{R}) \propto e^{-\mathcal{R}} \times \prod_{\text{triggers}} [\mathcal{R}(\text{trigger} | \mathcal{N}) + W(\text{trigger})\mathcal{R}], \quad (3)$$

where the product is over all the triggers in the bank, including those detected originally by the LVC. Using this likelihood, we compute a posterior on \mathcal{R} , assuming a uniform prior $P(\mathcal{R})$ between 0 and 50. For any value of the overall rate \mathcal{R} , we can calculate the probability that an event has astrophysical origin; our final quoted values were obtained by marginalizing over \mathcal{R} :

$$p_{\text{astro}}(\text{event}) = \int_0^\infty p_{\text{astro}}(\text{event} | \mathcal{R}) P(\mathcal{R}) d\mathcal{R}. \quad (4)$$

III. RESULTS ON THE PREVIOUSLY REPORTED EVENTS

Table I summarizes our pipeline’s results for the O2 events published by the LVC [2]. We detect all previously reported BBH events except for GW170608, for which the LVC did not provide the Hanford data in their bulk data release, and thus that time was not part of our coincidence search. We only report results from our BBH search in this paper, so we exclude the binary neutron star GW170817 from our results. Nearly all of the LVC events have only an upper limit for the FAR of $1/(20\,000\text{ O2})$. All of these events are certainly astrophysical sources with lower limit on $p_{\text{astro}} \geq 0.99$.

An interesting special case is GW170818, which was not found by the PyCBC pipeline, and deemed potentially interesting but not confirmed by the GstLAL pipeline using Hanford and Livingston alone [2]. It was subsequently detected with high confidence by GstLAL when Virgo data was included; we did not analyze Virgo for the search reported in this paper. Empirically, our background distributions do not have any louder L1 triggers than this event. The low score in H1, combined with the saturation of the L1 ranking scores $\tilde{\rho}_L^2$ at high SNR (see Figure 2), together imply that we need a more careful analysis to reliably assess the FAR and probability of astrophysical origin of such events. We defer this analysis to a follow-up paper, in which we will show that such events can be detected using the Livingston and Hanford detectors alone. In this subsequent work, we will also report the results of a search for similar events, i.e., events which are loud in one detector (and saturate the rank score), and which either have low scores in the other detectors, or have no coincident data.

IV. THE NEWLY DISCOVERED BBH MERGERS

Table II summarizes the basic properties of the newly discovered events: their parameters, FAR, and estimated probabilities of being of astrophysical origin, p_{astro} . We need the rate of astrophysical events in the detector, \mathcal{R} , to calculate these probabilities. We derive a distribution for \mathcal{R} from all the events we detected (which include those

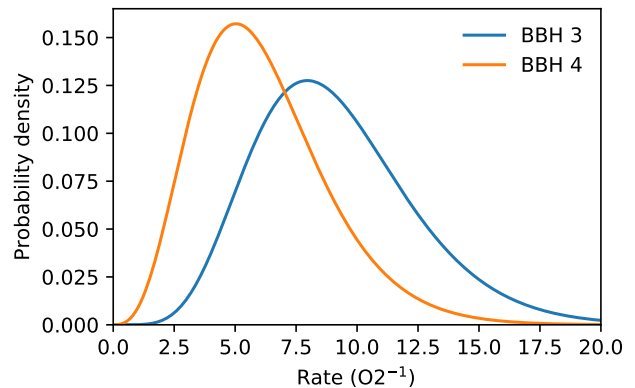


FIG. 3: Rates inferred from all the events. The rates are simplistic and bank-specific observed rates for black hole mergers, which we only use to determine the p_{astro} of the events. The rates are defined as the astrophysical occurrence rate of signals satisfying $\rho_{\text{H}}^2, \rho_{\text{L}}^2 > 16$ and $\rho_{\text{H}}^2 + \rho_{\text{L}}^2 > \rho_{\text{th}}^2$, where $\rho_{\text{th}}^2 = 60$ for BBH 3 and $\rho_{\text{th}}^2 = 57$ for BBH 4. The assumed network consists of two identical detectors with median Hanford sensitivity, observing in coincidence for 118 days. More careful analysis is required in order to infer astrophysically meaningful volumetric rates.

detected by the LVC analyses), and at the same time estimate the p_{astro} of each event, using the procedure described in Section II. Figure 3 shows the posteriors on the rates for chirp-mass banks BBH 3 and BBH 4; the values of $p_{\text{astro}}(\text{event})$ quoted in Tables I and II were marginalized over these posteriors.

Appendix A includes the posteriors for the parameters of all the new events. Figure 4 places these events in the context of the previous LVC events, as well as the one we reported in Ref. [17], by showing their distribution in the plane of source-frame total mass and the effective spin parameter χ_{eff} . In the remainder of this section, we briefly comment on the properties of each of the newly found events.

a. GW170121: This event has the lowest FAR among those not reported by the LVC ($\text{FAR}^{-1} \approx 2.8 \times 10^3 \text{ O2}$), and $p_{\text{astro}} > 0.99$. The posterior distribution of χ_{eff} has most of its support at negative values, $\chi_{\text{eff}} > 0$ being ruled out at the 95% confidence level. The chirp mass, mass-ratio and redshift of this event are similar to those of the heavy BBHs reported by the LVC. Its redshift is $z \sim 0.24$.

b. GW170304 & GW170727: These two events have $\text{FAR}^{-1} \sim 370 \text{ O2}$ and $p_{\text{astro}} \approx 0.98$. Their masses and spins are similar to those of the heavy BBHs detected by the LVC. Both events are consistent with zero χ_{eff} , and are on the massive end of the population. They have relatively high redshifts $z \sim 0.5$ and 0.43 , respectively.

c. GW170425: This candidate has $p_{\text{astro}} \approx 0.77$ and $\text{FAR}^{-1} \approx 29 \text{ O2}$. Its inferred parameters are similar to those of the heavy BBHs reported by the LVC; the effective spin χ_{eff} is consistent with zero. The posterior

TABLE I: Events already reported by the LIGO–Virgo Collaboration [2] as detected with our pipeline. The rate distributions used to compute p_{astro} are shown in Fig. 3. The maximum likelihood rates are $\mathcal{R}_{\text{max}} = 8/\text{O}2$ and $5/\text{O}2$ in banks BBH 3 and BBH 4, respectively.

Name	Bank	GPS time ^a	ρ_{H}^2	ρ_{L}^2	$\text{FAR}^{-1}(\text{O}2)^{\text{b}}$	$\frac{W(\text{event})}{\mathcal{R}(\text{event} \mathcal{N})}$ (O2)	p_{astro}
GW170104	BBH (3,0)	1167559936.582	85.1	104.3	$> 2 \times 10^4$	> 100	> 0.99
GW170809	BBH (3,0)	1186302519.740	40.5	113	$> 2 \times 10^4$	> 100	> 0.99
GW170814	BBH (3,0)	1186741861.519	90.2	170	$> 2 \times 10^4$	> 100	> 0.99
GW170818	BBH (3,0)	1187058327.075	19.4	95.1	1.7^{c}	—	— ^c
GW170729	BBH (3,1)	1185389807.311	62.1	53.6	$> 2 \times 10^4$	> 100	> 0.99
GW170823	BBH (3,1)	1187529256.500	46.0	90.7	$> 2 \times 10^4$	> 100	> 0.99

^a The times given are the ‘linear-free’ times of the best fit templates in our bank; with this time as the origin, the phase of the template is orthogonal to shifts in time, given the fiducial PSD.

^b The FARs given are computed within each bank; our BBH analysis has 5 chirp-mass banks. The inverse FAR is given in terms of ‘O2’ to reflect the volumetric weighting of events. Under the approximation of constant sensitivity of the detectors during the observing run, the unit ‘O2’ corresponds to ≈ 118 days.

^c See discussion in §III.

TABLE II: New events with astrophysical probability $> 50\%$ in all of the BBH banks. The rate distributions used to compute p_{astro} are shown in Fig. 3, the maximum-likelihood rates in banks BBH 3 and BBH 4 are $\mathcal{R}_{\text{max}} = 8/\text{O}2$ and $5/\text{O}2$, respectively.

Name	Bank	$\mathcal{M}^{\text{det}}(M_{\odot})$	χ_{eff}	z	GPS time ^a	ρ_{H}^2	ρ_{L}^2	$\text{FAR}^{-1}(\text{O}2)^{\text{b}}$	$\frac{W(\text{event})}{\mathcal{R}(\text{event} \mathcal{N})}$ (O2)	p_{astro}
GW170121	BBH (3,0)	29_{-3}^{+4}	$-0.3_{-0.3}^{+0.3}$	$0.24_{-0.13}^{+0.14}$	1169069154.565	29.4	89.7	2.8×10^3	> 30	> 0.99
GW170304	BBH (4,0)	47_{-7}^{+8}	$0.2_{-0.3}^{+0.3}$	$0.5_{-0.2}^{+0.2}$	1172680691.356	24.9	55.9	377	13.6	0.985
GW170727	BBH (4,0)	42_{-6}^{+6}	$-0.1_{-0.3}^{+0.3}$	$0.43_{-0.17}^{+0.18}$	1185152688.019	25.4	53.5	370	11.8	0.98
GW170425	BBH (4,0)	47_{-10}^{+26}	$0.0_{-0.5}^{+0.4}$	$0.5_{-0.3}^{+0.4}$	1177134832.178	28.6	37.5	15	0.65	0.77
GW170202	BBH (3,0)	$21.6_{-1.4}^{+4.2}$	$-0.2_{-0.3}^{+0.4}$	$0.27_{-0.12}^{+0.13}$	1170079035.715	26.5	41.7	6.3	0.25	0.68
GW170403	BBH (4,1)	48_{-7}^{+9}	$-0.7_{-0.3}^{+0.5}$	$0.45_{-0.19}^{+0.22}$	1175295989.221	31.3	31.0	4.7	0.23	0.56

^a The times given are the ‘linear-free’ times of the best fit templates in our bank; with this time as the origin, the phase of the template is orthogonal to shifts in time, given the fiducial PSD.

^b The FARs given are computed within each bank; our BBH analysis has 5 chirp-mass banks. The inverse FAR is given in terms of ‘O2’ to reflect the volumetric weighting of events. Under the approximation of constant sensitivity of the detectors during the observing run, the unit ‘O2’ corresponds to ≈ 118 days.

distribution has a tail extending to large values for the masses. Its inferred redshift is large, $z \sim 0.5$.

d. GW170202: This candidate has $p_{\text{astro}} \approx 0.7$ and $\text{FAR}^{-1} \approx 6 \text{O}2$. The masses and the spins are similar to those of the heavy LVC BBHs. It is found in the bank with the largest number of secure detections (BBH 3). It has a bimodal posterior, in which the solution with lower masses has a more negative spin, and is located closer. The inferred redshift is $z \sim 0.27$.

e. GW170403: This candidate has $\text{FAR}^{-1} \approx 5 \text{O}2$ and $p_{\text{astro}} \approx 0.55$; this is close to the threshold $p_{\text{astro}} = 0.5$ to make it into a list of detections (as defined in Ref. [2]). The inferred redshift is $z \sim 0.45$. Interestingly, the posterior for χ_{eff} is inconsistent with positive values.

In addition to these events, we list in Table III the sub-threshold triggers of our search, defined as those with $0.1 < p_{\text{astro}} < 0.5$. The sum of the p_{astro} of the events in this list exceeds unity; in fact, a candidate in bank BBH (4,1) has $p_{\text{astro}} \approx 0.45$, which is close to the detection threshold (though it has a relatively high $\text{FAR}^{-1} \approx 0.8 \text{O}2$). It is possible that an improved analysis, or rate-estimate, can push some of these candidates above the detection threshold.

V. SENSITIVITY OF OUR PIPELINE

In the previous section, we described several additional events we detected that are not in the catalog of events published by the LVC. All of these events pass the thresholds for detection in Ref. [2] (their FARs are above the threshold of 1 in 30 days, even accounting for the five banks in our BBH search, or eleven banks in a hypothetical binary neutron star and neutron-star–black-hole search [18]). This suggests that our search has a substantially larger sensitive volume.

Figure 5a shows the background triggers we collected using 20 000 time slides in those BBH sub-banks in which all the events considered in this work, both from the LVC and our analysis, reside. This figure does not include the BBHs from the O1 run (GW150914, GW151012, GW151216, GW151226), nor GW170608, which was not included in the bulk data release we analyzed. This figure is not intended as a demonstration of how we compute the FAR or p_{astro} for particular events: firstly, it shows ρ_{H}^2 and ρ_{L}^2 , i.e., the incoherent H1 and L1 SNR^2 , while we compute the FAR using a coherent score that takes into account the time-delays and the relative phases of the

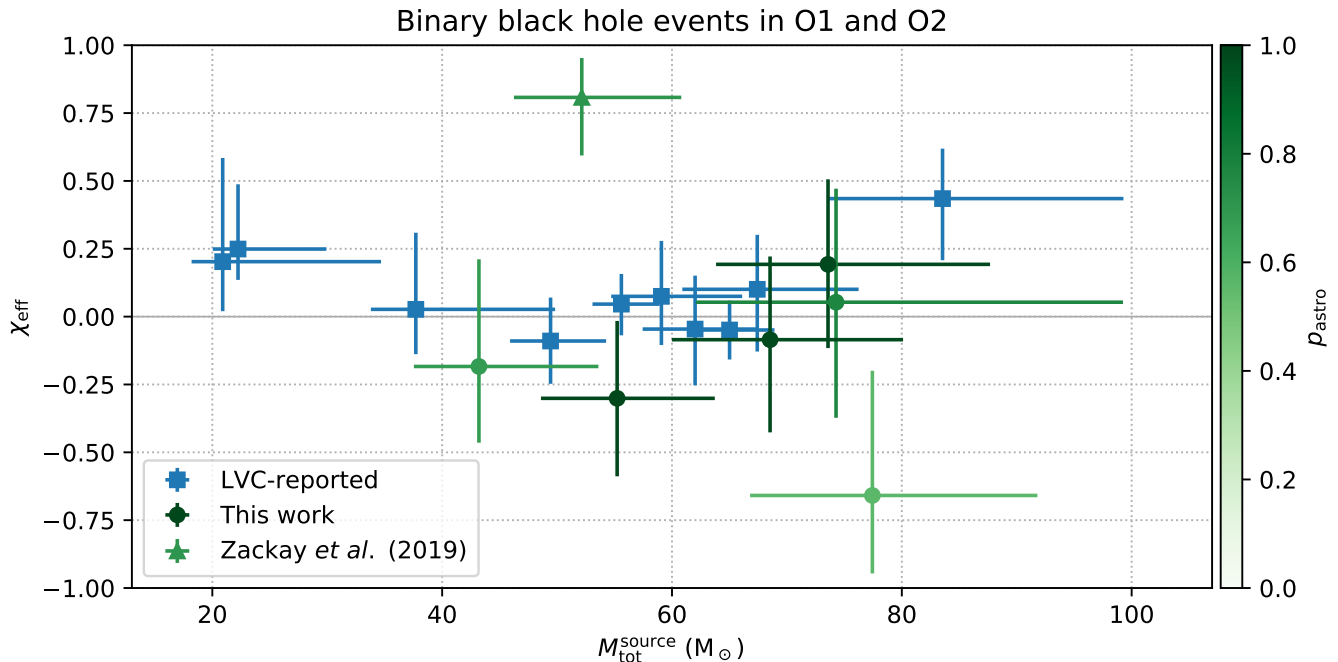


FIG. 4: Source-frame total mass and effective spin for the BBH events found in Hanford–Livingston coincidence, over O1 and O2. We recovered all the previously reported events with high confidence, $p_{\text{astro}} \approx 1$, except for GW170608 and GW170818, see §III. We found seven additional events ranging from marginal triggers to confident detections: one in O1 [17] and six in O2 (this work). The dots and error bars show median and 90% confidence intervals, respectively. The spin χ_{eff} and the mass can be correlated (not shown). The full posteriors can be found in Appendix A. The prior used was uniform in m_1 , m_2 , χ_{eff} , and luminosity volume.

TABLE III: Sub-threshold candidates with astrophysical probability above 10% in all of the BBH banks. The rate distributions used to compute p_{astro} are shown in Fig. 3, the maximum-likelihood rates in banks BBH 3 and BBH 4 are $\mathcal{R}_{\text{max}} = 8/\text{O2}$ and $5/\text{O2}$, respectively.

Bank	GPS time ^a	ρ_{H}^2	ρ_{L}^2	$\text{FAR}^{-1}(\text{O2})^{\text{b}}$	$\frac{W(\text{event})}{\mathcal{R}(\text{event} \mathcal{N})}(\text{O2})$	p_{astro}
BBH (4,1)	1172487817.477	48.6	19.1	0.82	0.147	0.45
BBH (3,0)	1170914187.455	20.4	41.4	0.43	0.044	0.28
BBH (3,1)	1172449151.468	29.5	32.4	0.31	0.025	0.18
BBH (4,0)	1174138338.385	37.1	28.4	0.62	0.034	0.17
BBH (3,0)	1171863216.108	46.5	21.6	0.27	0.016	0.125
BBH (3,1)	1187176593.222	20.3	42.0	0.2	0.014	0.12
BBH (3,0)	1182674889.044	34.1	28.7	0.23	0.016	0.12
BBH (3,1)	1171410777.200	40.8	21.0	0.18	0.014	0.11

^a The times given are the ‘linear-free’ times of the best fit templates in our bank; with this time as the origin, the phase of the template is orthogonal to shifts in time, given the fiducial PSD.

^b The FARs given are computed within each bank; our BBH analysis has 5 chirp-mass banks. The inverse FAR is given in terms of ‘O2’ to reflect the volumetric weighting of events. Under the approximation of constant sensitivity of the detectors during the observing run, the unit ‘O2’ corresponds to ≈ 118 days.

triggers, and the differing detector sensitivities; secondly, we estimate the FAR and the p_{astro} for a particular event using the background in its chirp-mass bank, and sub-bank, respectively. We include this figure only to easily visualize the sensitive volume. The solid and dashed lines show the approximate detection thresholds for different analyses (with the above caveat on the validity of incoherent thresholds). The detection thresholds shown for the LVC catalog are approximate and conservative, they

err on the side of reporting a better sensitivity for the standard pipeline. At the single-detector level, we set the threshold by the non-detection of GW170121 (the PyCBC pipeline has an explicit cut on single-detector $\text{SNR} = 5.5$ [11]). We set the minimum network $\text{SNR}^2 = \rho_{\text{H}}^2 + \rho_{\text{L}}^2 > 90$ by scaling the reported FAR of GW170729 to $1/\text{O2}$, and rounding down.

It is clear from Fig. 5 that our pipeline has substantially lower background in the relevant region: for exam-

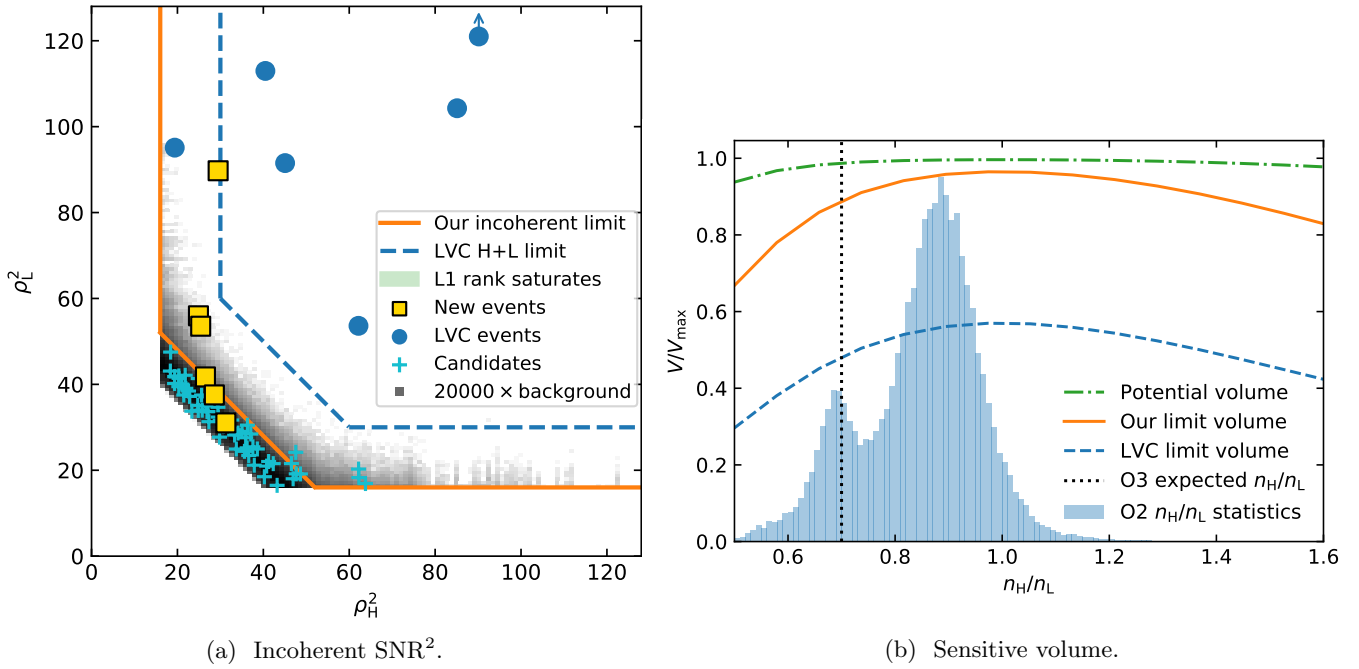


FIG. 5: *Left*: Incoherent Hanford and Livingston SNR² for coincident and background triggers (computed using 2×10^4 time slides), for all the sub-banks where there are events. The blue and orange lines are approximate incoherent detection limits for the LVC and the current analysis, respectively, restricted to using Hanford and Livingston data only (see text for caveats). GW170814 has $\rho_L^2 = 170$, higher than shown here (indicated with an arrow). GW170608 is not shown, see §III. *Right*: The lines show the (incoherent) volume probed by different analyses as a function of the Hanford and Livingston detector sensitivities, at fixed network total sensitivity. The orange (solid) and blue (dashed) curves show the estimated volume probed by the present and LVC analyses, respectively. The green, dashed-dotted curve shows the potential volume that can be opened up by analyzing interesting single-detector triggers. The shaded histogram shows the distribution of $V \times T$, i.e., the product of the sensitive volume and the time, as a function of the sensitivity ratios between the Hanford and Livingston detectors in the O2 run, as measured by our analysis. The O3 run, as reported in Ref. [20], has begun with a sensitivity ratio $n_H/n_L \approx 0.7$.

ple, we see no background triggers within the sensitive region of the standard pipelines. All but one of the LVC reported events have values of ρ_L^2 that are so large that we do not have even single-detector background triggers at their level (this is a consequence of our data-cleaning procedure, as well as our signal-quality vetoes). The only exception to this is GW170729, with $(\rho_H^2, \rho_L^2) = (62, 53)$. This event had FARs of 0.2 yr^{-1} and 1.36 yr^{-1} in the GstLAL and PyCBC pipelines, respectively, but we have no background in its vicinity even incoherently (i.e., allowing for arbitrary phases, time-delays, and sensitivity ratios of the two detectors).

The difference in the detection limits, at the same threshold on FAR, maps to a difference in the sensitive volume between the searches. The size of this difference depends on the ratio of the sensitivities of the two detectors we analyze, i.e., H1 and L1. The sensitivities n_H and n_L are proportional to the SNR with which a gravitational wave signal with a given strain amplitude is measured by H1 and L1, respectively. Figure 5b shows the volume as a function of the sensitivity ratio (scaled such that a volume of V_{max} corresponds to detecting all events with $\rho_H^2 + \rho_L^2 > 68$); the solid orange and the

dashed blue lines are for the cuts shown in Fig. 5a. The curves were obtained by randomizing the angular locations and inclinations of a large number of mergers on the sky and recording the incoherent scores (including the stochastic noise contribution) at the detectors with a given sensitivity-ratio. We see that the orange curve gains approximately a factor of two in sensitive volume. In particular, note that the gain is larger when the sensitivities of the detectors are very different. The filled histogram in Figure 5b shows the distribution of the ratio of the Hanford and Livingston sensitivities in our analysis of the O2 run, weighted by the momentary space-time volume. We estimate this by approximating the detection regions of the different analyses. The LVC H+L limit was approximated by $\rho_H^2 + \rho_L^2 > 90$ and $\rho_H^2, \rho_L^2 > 30$. Our incoherent limit was approximated as $\rho_H^2 + \rho_L^2 > 68$, and $\rho_H^2, \rho_L^2 > 16$.

Also of particular interest is the limit in which the SNR is much larger in one detector than in the other. For part of the O2 run, the Livingston detector was substantially more sensitive than the Hanford one, and hence there is a substantial phase-space volume for astrophysical signals to have disparate SNR in the detectors. Figure 5a

shows that there is substantially less background in L1 in the high SNR regime (see the teal shaded region). The few background events in this region come from the same small number of loud events in L1 matching with Gaussian fluctuations in H1 at different time shifts, and hence the ranking function $\tilde{\rho}_L^2$ saturates and is severely affected by Poisson noise (see Fig. 2). We need a different analysis to estimate a meaningful FAR in this regime; the green, dashed-dotted curve in Figure 5b shows that we can gain a non-trivial amount of sensitive volume if we open up this region. We will study this regime in more detail in a subsequent paper, in which we will introduce a formalism for searching for events and assessing the FAR in this region. Notably, the LVC event GW170818, which was detected using Virgo data, belongs to this category.

VI. CONCLUSIONS

In this paper we presented the results of our search for BBHs in the data from the O2 observing run of advanced LIGO, using the methods introduced in our work in Ref. [1]. We report six new events above the detection thresholds defined by the LVC (in terms of FAR and p_{astro}), three of whom have probability $p_{\text{astro}} > 0.98$ of being of astrophysical origin. Interestingly, all the new events are in banks BBH 3 and BBH 4 (our heavy chirp-mass banks), as are most of the ones reported by the LVC.

The most significant new event (GW170121) prefers negative χ_{eff} and is inconsistent with positive values at the 95% level. The most marginal candidate event (GW170403), with $p_{\text{astro}} \sim 0.5$, is inconsistent with zero or positive χ_{eff} . The spin of the merging BBHs is an important discriminator between formation channels [21]. Hence, the new events presented in this work can throw light on the mechanisms by which BBHs are assembled.

More generally, with the increased number of events, the clear next step is to perform a population analysis that accounts for selection biases, which will map out the distribution of the intrinsic parameters of the mergers. In particular, including new events in population analyses can significantly inform us about the dependence of the merger-rate on mass and redshift.

The LVC recently started their third observing run (O3), and several new detections are expected in the near future. The new events we report in this paper show that there will be additional information in the LIGO and Virgo data in addition to what the pipelines used by the LVC currently extract. The development of our pipeline has been facilitated by access to the public O1 and O2 data, as well as the LIGO Algorithm Library [22]. We thank the LVC for releasing the data and tools to the community. We hope that data from current and future runs can be made available quickly to incentivize external groups to develop new analysis methods and maximize the scientific yield of the LVC data.

ACKNOWLEDGEMENTS

This research made use of data, software and/or web tools obtained from the Gravitational Wave Open Science Center (<https://www.gw-openscience.org>), a service of LIGO Laboratory, the LIGO Scientific Collaboration and the Virgo Collaboration. LIGO is funded by the U.S. National Science Foundation. Virgo is funded by the French Centre National de Recherche Scientifique (CNRS), the Italian Istituto Nazionale della Fisica Nucleare (INFN) and the Dutch Nikhef, with contributions by Polish and Hungarian institutes.

TV acknowledges support by the Friends of the Institute for Advanced Study. BZ acknowledges the support of The Peter Svennilsson Membership fund. LD acknowledges the support from the Raymond and Beverly Sackler Foundation Fund. MZ is supported by NSF grants AST-1409709, PHY-1521097 and PHY-1820775 the Canadian Institute for Advanced Research (CIFAR) program on Gravity and the Extreme Universe and the Simons Foundation Modern Inflationary Cosmology initiative.

Appendix A: Posteriors for the intrinsic parameters of the new events

Figures 6 and 7 show the marginalized posterior distributions of detector-frame chirp mass, mass-ratio, effective spin, and redshift for the new events reported with $p_{\text{astro}} > 0.5$. We obtained the distributions using a prior that is uniform in m_1 , m_2 , χ_{eff} and luminosity volume, as detailed in Ref. [17]. The search used only data from Hanford and Livingston, but we computed posteriors for each event by coherently analyzing the data from all detectors available (Hanford, Livingston and/or Virgo). We evaluated the likelihood using the relative binning method [23], and used the IMRPhenomD waveform model [24]. We used the PyMultiNest sampler to generate the posteriors [25].

Appendix B: Populating events in sub-banks and banks

A single signal or noise transient produces triggers in several sub-banks, and even across chirp-mass banks. We ultimately assign events to a single sub-bank within a single chirp-mass bank. In order to come up with a reasonable criterion for this assignment, we should consider the distribution of the triggers given a signal in the data.

In our search, we first collect coincident triggers (triggers with templates indexed by the same coefficients c_α , and within 10 ms of each other) above a threshold. We then veto the H1 and L1 triggers, refine them on a finer c_α grid, and pick the best coincident trigger from the subsets of refined H1 and L1 triggers: every step involved shapes the distributions of the final triggers.

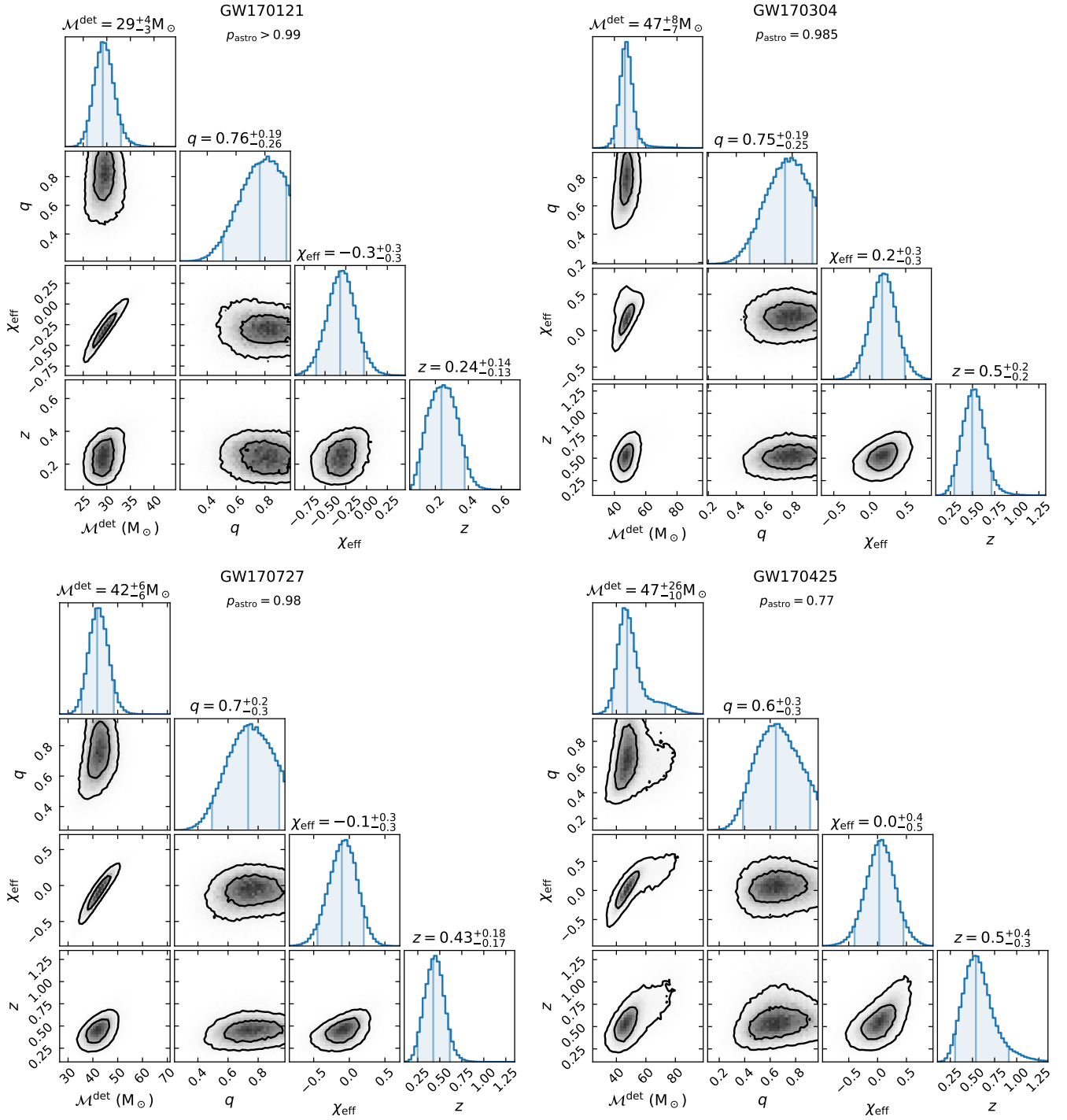


FIG. 6: Marginalized posteriors for the new events reported in this work (continued in Fig. 7). Two-dimensional contours enclose 50% and 90% of the distribution. In the one-dimensional posteriors, vertical lines show the 0.05, 0.5 and 0.95 quantiles. The prior used is uniform in detector-frame m_1 , m_2 , χ_{eff} and luminosity volume. The waveform model used is IMRPhenomD [24].

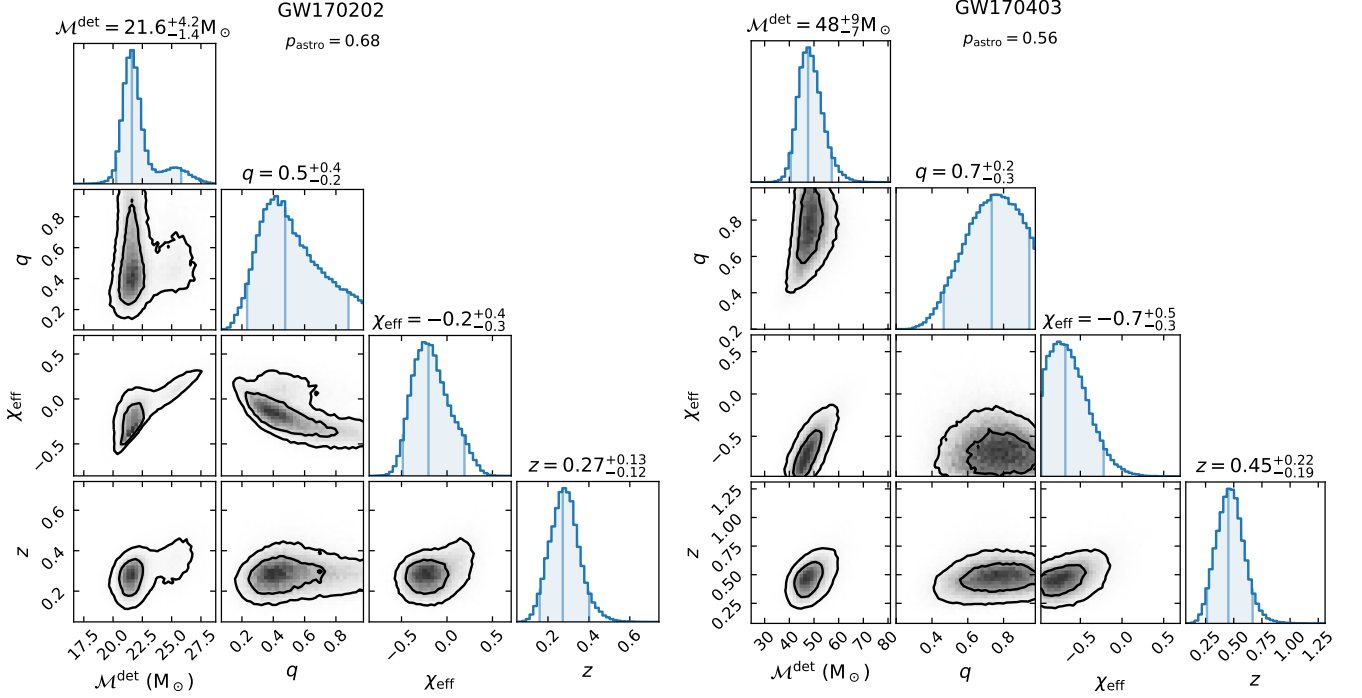


FIG. 7: Continuation of Fig. 6 displaying marginalized posteriors for GW170202 and GW170403.

For simplicity, let us start with triggers in a single detector. Let d denote the strain data, A be the signal amplitude, and Θ be the other parameters of the signal: these include the coefficients $c_{\alpha,i}$ in sub-bank i of chirp-mass bank B , and the phase and the merger-time. The likelihood of the sub-bank i under the signal hypothesis is

$$\mathcal{L}(d | i, B, S) = \sum \iint d\Theta dA p(\Theta) p(A) \mathcal{L}(d | A, \Theta), \quad (\text{B1})$$

where the sum runs over the grid points in $c_{\alpha,i}$, and the integral is over continuous parameters (time and phase). We can view the sum over the coefficients $c_{\alpha,i}$ as a Riemann sum for an integral over the underlying continuous space, \mathcal{V} , and thus approximate Eq. (B1) as

$$\begin{aligned} \mathcal{L}(d | i, B, S) \\ \approx \frac{1}{(\Delta c_{\alpha,i})^{n_{c_{\alpha,i}}}} \iint d\Theta dA p(A) p(\Theta) p(A) \mathcal{L}(d | A, \Theta), \end{aligned} \quad (\text{B2})$$

where $\Delta c_{\alpha,i}$ and $n_{c_{\alpha,i}}$ are the spacing and dimensionality of the template grid in sub-bank i . The factor in front of the integral is the volume per template in the discrete grid.

We adopt the following assumptions:

1. In the prior $p(\Theta)$, astrophysical signals are equally likely to occur in two different chirp-mass banks.

2. The astrophysical rate per template is uniform within a chirp-mass bank, i.e., given that a signal occurs within bank B , the probability that it occurs with a given template equals $1/N_{\text{temp},B} = 1/\sum_i N_{\text{temp},i}$, where $N_{\text{temp},B}$ and $N_{\text{temp},i}$ are the number of templates in the bank B and sub-bank i , respectively (we make the same assumption when estimating the detector rate of events in Section II).

3. The integral in Eq. (B2) receives most its contribution from around the best fit parameters, Θ_* , and amplitude A_* , which is valid in the limit of high SNR.

The merger-time and phase are uniformly distributed within their ranges, while the amplitude has a prior distribution $p(A) \sim 1/A^4$ in a Euclidean universe. The integrand $\mathcal{L}(d | A, \Theta)$ has the form

$$\mathcal{L}(d | A, \Theta) = \exp \left[-\frac{\langle d - At(\Theta) | d - At(\Theta) \rangle}{2} \right], \quad (\text{B3})$$

where $t(\Theta)$ is the template, and the inner product is weighted by the inverse PSD. Next, we integrate over the amplitude in Eq. (B2). Under assumption 3 above, this gives us a prefactor A_*^{-4} , and simplifies the integrand to

$$\mathcal{L}(d | \Theta) \propto \exp \left[\frac{\langle d | t(\Theta) \rangle^2}{2 \langle t(\Theta) | t(\Theta) \rangle} \right], \quad (\text{B4})$$

where we have removed a term that does not depend on the templates (this step is identical to the standard

derivation of the \mathcal{F} -statistic [26]). We express the best fit amplitude as $A_* = (\rho/\rho_0)A_0$, where ρ_0 is the SNR of a merger at a fiducial distance and orientation, which captures the instantaneous sensitivity of the detector.

By assumption 3 above, the integrand in Eq. (B4) is sharply peaked around the bestfit parameters Θ_0 , there it equals $\exp(\rho^2/2)$, where $\rho^2 = \langle A_* t(\Theta) | A_* t(\Theta) \rangle$ is the SNR². A nice feature of our template banks is that the deviation in coefficients, δc_α , directly measures the degradation in the overlap between templates [18]:

$$\langle A_* t(c_\alpha) | A_* t(c_{\alpha,0}) \rangle \approx \rho^2 \left(1 - \frac{\delta c_\alpha^2}{2} \right). \quad (\text{B5})$$

A similar relation holds for the other continuous parameters (time and phase), i.e the degradation in overlaps is quadratic with displacement (the principal directions are some linear combinations of time and phase), and the width is inversely related to ρ . We simplify the integrand of Eq. (B4), substitute it into Eq. (B2), and use the prior on the templates from assumptions 1 and 2 to obtain

$$\begin{aligned} \mathcal{L}(d | i, B, \mathcal{S}) & \propto \frac{(\rho/\rho_0)^{-4}}{N_{\text{temp},B}(\Delta c_{\alpha,i})^{n_{c_{\alpha,i}}}} \iint d\delta\Theta \exp \left[\frac{\rho^2}{2} (1 - \delta\Theta^2) \right] \\ & = \frac{(\rho/\rho_0)^{-4} \exp(\rho^2/2)}{N_{\text{temp},B}(\Delta c_{\alpha,i})^{n_{c_{\alpha,i}}}} \left(\frac{2\pi}{\rho^2} \right)^{(n_{\Theta} \equiv (n_{c_{\alpha,i}} + 2))/2}. \end{aligned} \quad (\text{B6})$$

When we refine coincident triggers between two detectors, the Θ contains four extra parameters apart from the template coefficients: two times, and two phases. A complication is that astrophysical signals are not uniformly distributed in the space of the time delay and relative phase, and the distribution depends on the relative sensitivities of the two detectors, $\rho_{0,H}/\rho_{0,L}$. Thus there is a nontrivial prior in the space of parameters Θ .

We make progress by noting that the likelihood in the integrand in Eq. (B2) is independent of the relative times and phases. In this case, we are greatly helped by our assumption 3 above, which tells us that all we need is to evaluate the prior at the bestfit parameters Θ_* . We combine the prior and amplitude prefactor together into a function $p(\Delta t, \Delta\phi, \rho_H^2, \rho_L^2 | \rho_{0,H}, \rho_{0,L})$, which we evaluate by Montecarlo sampling methods.

The integral over the likelihood in Eq. (B2) can be evaluated in a similar manner as above, with the difference that now $\rho^2 = \rho_H^2 + \rho_L^2$. Thus we finally obtain

$$\begin{aligned} \mathcal{L}(d_H, d_L | i, B, \mathcal{S}) & \propto \frac{p(\Delta t, \Delta\phi, \rho_H^2, \rho_L^2 | \rho_{0,H}, \rho_{0,L}) e^{\rho^2/2}}{N_{\text{temp},B}(\Delta c_{\alpha,i})^{n_{c_{\alpha,i}}}} \left(\frac{2\pi}{\rho^2} \right)^{(n_{c_{\alpha,i}} + 4)/2} \end{aligned} \quad (\text{B7})$$

Note that the exponent of the last term is different due to the extra degrees of freedom in the two-detector case.

We use the ratio of the likelihoods given by Eq. (B7) as a discriminator to compare triggers in the same location in different sub-banks (and possibly chirp-mass-banks).

Appendix C: Definition of rank functions in different sub-banks

We compute FARs of events by comparing them to background triggers in their chirp-mass bank. An essential ingredient in this computation is the likelihood $\mathcal{L}(t | \mathcal{N})$ for a trigger t under the noise hypothesis. Coincident triggers are produced with random time-delays and relative phases between the two detectors, and the likelihood $\mathcal{L}(t | \mathcal{N})$ depends only on the incoherent SNR² in the two detectors, and the template in sub-bank i (which we denote by the set of coefficients c_α of the basis phase functions), i.e., $\mathcal{L}(t | \mathcal{N}) = P(\rho_H^2, \rho_L^2, c_\alpha, i)$. We can write:

$$P(\rho_H^2, \rho_L^2, c_\alpha, i) = P(\rho_H^2, \rho_L^2, c_\alpha | i) P(i) \quad (\text{C1})$$

$$= \frac{P(\rho_H^2 | i) P(\rho_L^2 | i)}{N_{\text{temp},i}} P(i), \quad (\text{C2})$$

where $P(i)$ is the probability that noise produces a coincident trigger in sub-bank i , regardless of the SNR², and $N_{\text{temp},i}$ is the number of templates in sub-bank i .

Equation (C2) assumes that a) the background is flat over templates within each sub-bank, and b) the triggers in different detectors are independent of each other. Both these assumptions fail to some degree (the latter happens because we refine coincident triggers, and pick the best common template). One solution would be to directly estimate the probability in Eq. (C1) from the background, but in practice, the many-dimensional distribution is hard to sample finely enough, and thus real coincident triggers can receive spurious penalties to their scores. We use the same assumptions to rank the time slides as well as the coincident triggers, and hence our FARs are not biased for the strategy we adopt; the price of the above assumptions is that our ranking is no longer strictly optimal.

The probability $P(i)$ is

$$P(i) = \frac{N_{\text{trig},i}}{N_{\text{trig}}}, \quad (\text{C3})$$

where $N_{\text{trig},i}$ is the number of triggers in sub-bank i , and N_{trig} is the number of triggers summed over all sub-banks.

We approximate the probability $P(\rho^2 | i)$ for each detector using the same ranking function that we adopted in our previous work [1], but compute it separately for each sub-bank:

$$\frac{P(\rho^2 | i)}{P(\rho_0^2 | i)} \approx \frac{\text{Rank}(\rho^2 | i)}{\text{Rank}(\rho_0^2 | i)}, \quad (\text{C4})$$

where $\text{Rank}(\rho^2 | i)$ is the ranking of a given trigger in its sub-bank (with the lowest rank given to the loudest event) and ρ_0^2 is a normalization point that we set to $\rho_0^2 \approx 30$. We estimate $P(\rho_0^2 | i)$ by taking the ratio between the number of triggers in a bin around ρ_0^2 in

sub-bank i over the total number of triggers in the sub-bank, i.e.,

$$P(\rho_0^2 | i) \propto -\frac{1}{N_{\text{trig},i}} \frac{d}{d\rho^2} \text{Rank}(\rho^2 | i) \Big|_{\rho=\rho_0}. \quad (\text{C5})$$

-
- [1] T. Venumadhav, B. Zackay, J. Roulet, L. Dai, and M. Zaldarriaga, arXiv e-prints, arXiv:1902.10341 (2019), arXiv:1902.10341 [astro-ph.IM].
- [2] B. P. Abbott *et al.* (LIGO Scientific, Virgo), (2018), arXiv:1811.12907 [astro-ph.HE].
- [3] B. P. Abbott *et al.* (LIGO Scientific Collaboration and Virgo Collaboration), Physical Review Letters **116**, 061102 (2016).
- [4] B. P. Abbott *et al.* (LIGO Scientific Collaboration and Virgo Collaboration), Physical Review Letters **116**, 241103 (2016).
- [5] B. P. Abbott *et al.* (LIGO Scientific Collaboration and Virgo Collaboration), Phys. Rev. X **6**, 041015 (2016).
- [6] B. P. Abbott *et al.* (LIGO Scientific and Virgo Collaboration), Phys. Rev. Lett. **118**, 221101 (2017).
- [7] B. P. Abbott *et al.*, The Astrophysical Journal **851**, L35 (2017).
- [8] B. P. Abbott *et al.* (LIGO Scientific Collaboration and Virgo Collaboration), Physical Review Letters **119**, 141101 (2017).
- [9] B. P. Abbott *et al.* (LIGO Scientific Collaboration and Virgo Collaboration), Phys. Rev. Lett. **119**, 161101 (2017).
- [10] K. Chatziioannou, R. Cotesta, S. Ghonge, J. Lange, *et al.*, arXiv e-prints, arXiv:1903.06742 (2019), arXiv:1903.06742 [gr-qc].
- [11] S. A. Usman, A. H. Nitz, I. W. Harry, C. M. Biwer, *et al.*, Classical and Quantum Gravity **33**, 215004 (2016), arXiv:1508.02357 [gr-qc].
- [12] S. Sachdev, S. Caudill, H. Fong, R. K. L. Lo, *et al.*, (2019), arXiv:1901.08580v1 [gr-qc].
- [13] S. Klimentenko, G. Vedovato, M. Drago, F. Salemi, *et al.*, Phys. Rev. D **93**, 042004 (2016).
- [14] A. H. Nitz, C. Capano, A. B. Nielsen, S. Reyes, R. White, D. A. Brown, and B. Krishnan, arXiv e-prints, arXiv:1811.01921 (2018), arXiv:1811.01921 [gr-qc].
- [15] “Gravitational Wave Open Science Center (GWOSC),” www.gw-openscience.org/02/ (accessed 2019-02-27).
- [16] M. Vallisneri, J. Kanner, R. Williams, A. Weinstein, and B. Stephens, in *Journal of Physics Conference Series*, Journal of Physics Conference Series, Vol. 610 (2015) p. 012021, arXiv:1410.4839 [gr-qc].
- [17] B. Zackay, T. Venumadhav, L. Dai, J. Roulet, and M. Zaldarriaga, arXiv e-prints, arXiv:1902.10331 (2019), arXiv:1902.10331 [astro-ph.HE].
- [18] J. Roulet, L. Dai, T. Venumadhav, B. Zackay, and M. Zaldarriaga, arXiv e-prints, arXiv:1904.01683 (2019), arXiv:1904.01683 [astro-ph.IM].
- [19] A. H. Nitz, T. Dent, T. Dal Canton, S. Fairhurst, and D. A. Brown, Astrophys. J. **849**, 118 (2017), arXiv:1705.01513 [gr-qc].
- [20] “Gravitational Wave Open Science Center detector status,” www.gw-openscience.org/detector_status/day/20190412/ (accessed 2019-04-12).
- [21] B. Farr, D. E. Holz, and W. M. Farr, Astrophys. J. **854**, L9 (2018), arXiv:1709.07896 [astro-ph.HE].
- [22] LIGO Scientific Collaboration, “LIGO Algorithm Library - LALSuite,” free software (GPL) (2018).
- [23] B. Zackay, L. Dai, and T. Venumadhav, arXiv e-prints (2018), arXiv:1806.08792 [astro-ph.IM].
- [24] S. Khan, S. Husa, M. Hannam, F. Ohme, M. Pürrer, X. J. Forsteza, and A. Bohé, Physical Review D **93** (2016), 10.1103/physrevd.93.044007.
- [25] J. Buchner, A. Georgakakis, K. Nandra, L. Hsu, *et al.*, Astronomy & Astrophysics **564**, A125 (2014).
- [26] P. Jaranowski and A. Królak, Living Reviews in Relativity **15**, 4 (2012).